



Young, A. W., Eckner, W. J., Milner, W. R., Kedar, D., Norcia, M. A., Oelker, E., Schine, N., Ye, J. and Kaufman, A. M. (2020) Half-minute-scale atomic coherence and high relative stability in a tweezer clock. *Nature*, 588, pp. 403-413.

There may be differences between this version and the published version. You are advised to consult the publisher's version if you wish to cite from it.

<http://eprints.gla.ac.uk/224122/>

Deposited on 20 October 2020

1 Half-minute-scale atomic coherence and high relative stability in

2 a tweezer clock

Aaron W. Young, William J. Eckner, William R. Milner, Dhruv Kedar, Matthew

A. Norcia, Eric Oelker, Nathan Schine, Jun Ye, and Adam M. Kaufman*

*JILA, University of Colorado and National Institute of Standards and Technology,
and Department of Physics, University of Colorado, Boulder, Colorado 80309, USA*

(Dated: September 9, 2020)

Abstract

9 The preparation of large, low-entropy, highly coherent ensembles of identical quantum systems is
 10 foundational for many studies in quantum metrology [1], simulation [2], and information [3]. Here,
 11 we realize these features by leveraging the favorable properties of tweezer-trapped alkaline-earth
 12 atoms [4–6] while introducing a new, hybrid approach to tailoring optical potentials that balances
 13 scalability, high-fidelity state preparation, site-resolved readout, and preservation of atomic coher-
 14 ence. With this approach, we achieve trapping and optical clock excited-state lifetimes exceeding
 15 40 seconds in ensembles of approximately 150 atoms. This leads to half-minute-scale atomic co-
 16 herence on an optical clock transition, corresponding to quality factors well in excess of 10^{16} .
 17 These coherence times and atom numbers reduce the effect of quantum projection noise to a level
 18 that is on par with leading atomic systems [7, 8], yielding a relative fractional frequency stability
 19 of $5.2(3) \times 10^{-17} (\tau/s)^{-1/2}$ for synchronous clock comparisons between sub-ensembles within the
 20 tweezer array. When further combined with the microscopic control and readout available in this
 21 system, these results pave the way towards long-lived engineered entanglement on an optical clock
 22 transition [9] in tailored atom arrays.

23 A key requirement in quantum metrology, simulation, and information is the control
24 and preservation of coherence in large ensembles of effective quantum two level systems, or
25 qubits [1–3]. One way to realize these features is with neutral atoms [10, 11], which benefit
26 from being inherently identical, and having weak and short-range interactions in their ground
27 states. This, combined with the precise motional and configurational control provided by
28 tailored optical potentials, enables assembly of large ensembles of atomic qubits [12–15]
29 without the need for careful calibration of individual qubits or additional shielding from
30 uncontrolled interactions with the environment. As a result, groundbreaking work has been
31 done in such systems using alkali atoms, including the realization of controllable interactions
32 and gates [16, 17], preparation of useful quantum resources [18], and simulation of various
33 spin models of interest [19, 20]. These techniques have recently been extended to alkaline-
34 earth (or alkaline-earth-like) atoms [4–6, 21], which further provide access to extremely long-
35 lived nuclear and electronic excited states, and new schemes for Rydberg spectroscopy [22].

36 These recent advancements have enabled the development of tweezer-array optical
37 clocks [23, 24], which leverage the flexible potentials provided by optical tweezer arrays
38 to rapidly prepare and interrogate ensembles of many non-interacting atoms. As a result,
39 these clocks can balance the pristine isolation and high duty cycles available in single ion-
40 based optical clocks [25, 26] with the large ensembles and resultant low quantum projection
41 noise (QPN) available in optical lattice clocks [1, 7, 8, 27]. The most stable tweezer clock
42 demonstrated to date used a one-dimensional (1D) array containing 5 atoms, and conse-
43 quently was limited by QPN to a stability of $4.7 \times 10^{-16} (\tau/s)^{-1/2}$ [24], about an order of
44 magnitude worse than the record values of $3.1 \times 10^{-17} (\tau/s)^{-1/2}$ reported for synchronous
45 comparisons in a 3D lattice clock [7], and $4.8 \times 10^{-17} (\tau/s)^{-1/2}$ for a comparison between
46 two clocks [8]. Extending tweezer-array clocks to large 2D arrays helps to close this gap by
47 increasing atom number while maintaining the high duty cycles achievable in tweezer-based
48 systems [24].

49 The tweezer-clock architecture also benefits from microscopic single-particle control
50 through 100-nanometer-precision positioning of individual atoms. Such control can help
51 to probe and protect against the mechanisms that influence quantum coherence in neutral
52 atom clocks, such as interactions, tunneling, and spontaneous emission [28]. This capability,
53 combined with a series of other advances, allows us to realize sub-hertz control of an optical
54 clock transition in a tweezer array of 320 traps containing a total of on average ~ 150 atoms

55 (see Fig. 1). We demonstrate the ability to load ground-state cooled atoms into shallow
56 clock-magic tweezers, achieving excited-state lifetimes of up to 46(5) seconds and clock fre-
57 quency homogeneity on the scale of tens of millihertz across all tweezers. As a consequence,
58 we measure a coherence time of 19.5(8) s for synchronous frequency comparisons involving
59 the entire array, and observe evidence of atomic coherence out to 48(8) seconds for select
60 atoms in the array, corresponding to an atomic quality factor (Q) of $6.5(1.1) \times 10^{16}$. These
61 characteristics reduce the effects of QPN in the tweezer clock platform to a level that is
62 on par with the state of the art [7, 8], yielding a relative fractional frequency stability of
63 $5.2(3) \times 10^{-17} (\tau/s)^{-1/2}$ for synchronous self-comparisons.

64 A central challenge for using tweezer-array systems in quantum science is maintaining
65 control while scaling to larger atom numbers, since the required optical power scales linearly
66 with the system size. Our solution is to use several optical potentials optimized for different
67 stages of the experiment, and to realize state-preserving, low-loss transfer between these
68 different potentials [29]. We use an “auxiliary” potential composed of both a tweezer array
69 and an optical lattice for initial state preparation and readout, and a “science” potential
70 for clock interrogation, which is composed of a tweezer array that is at a magic wavelength
71 for the clock transition (see Fig. 1a, c). The auxiliary potential efficiently generates many
72 deep traps that allow for high-fidelity ground-state cooling of large ensembles of atoms. By
73 pre-cooling the atoms, the power requirements on the science potential are greatly relaxed,
74 and no longer poses a limitation on atom number or state preparation.

75 To confirm that the atoms remain cold when transferring them between these potentials
76 we perform sideband thermometry [5], first in the auxiliary potential (including the lattice)
77 immediately after sideband cooling, and then after adiabatically passing the atoms to the
78 science potential, holding for 25 ms, and passing them back [30]. With optimal alignment,
79 this whole “handoff” procedure can be performed with 0.0(3)% additional atom loss [30].
80 As shown in Fig. 1d, before the handoff we observe an average phonon occupation of $\bar{n} =$
81 $0.07_{-0.07}^{+0.14}$, $0.06_{-0.06}^{+0.08}$, and 0.07 ± 0.06 in the axial, first, and second radial directions respectively.
82 After the handoff these occupations are $\bar{n} = 0.25 \pm 0.12$, 0.31 ± 0.13 , and 0.27 ± 0.10 . Since
83 we expect that heating occurs during both steps of the handoff, the mean of these two
84 measurements serves as an estimate of the temperature of the atoms in the science potential.
85 In a smaller 6×6 region at the center of the array the axial cooling and handoff performance
86 is vastly improved, with an average phonon occupation of $\bar{n} = 0.00_{-0.00}^{+0.06}$ ($\bar{n} = 0.06_{-0.06}^{+0.10}$) before

87 (after) the handoff [30].

88 These low temperatures allow for clock operation in shallow tweezers, which both im-
89 proves scalability and minimizes clock decoherence due to Raman-transitions driven by the
90 trap photons [28, 31]. Specifically, in $25E_R$, or $4.3 \mu\text{K}$ deep tweezers (where E_R is the recoil
91 energy associated with a single 813 nm photon) — barely a quarter of the shallowest depths
92 reported in previous works [24] — we observe trap lifetimes of $160(10)$ s (Fig. 2a), likely
93 limited by our vacuum. At this depth we measure Fourier-limited spectroscopic features on
94 the $^1S_0 \leftrightarrow ^3P_0$ optical clock transition with linewidths as low as $0.62(1)$ Hz (full width at
95 half maximum) averaged across all tweezers, with inhomogeneous broadening on the scale
96 of tens of millihertz [30] (Fig. 1e).

97 Unlike in lattice clocks, where the effects of tunneling can become limiting at depths
98 below $\sim 30E_R$ along a single axis ($\sim 100E_R$ in a 3D lattice) [28], we observe no evidence
99 of tunneling or thermal hopping in tweezers as shallow as $6E_R$ [30]. Importantly, at this
100 depth we calculate the tunneling rate to be ~ 1 Hz, suggesting that disorder also plays a
101 key role in pinning the atoms. While this is encouraging, at these depths other sources of
102 atom loss [30] begin to limit our trap lifetime to far below $160(10)$ s. A competition between
103 these losses and Raman scattering leads to an optimal trap depth with respect to clock-state
104 lifetime of $\sim 14E_R$, where we measure a lifetime of $46(5)$ s (Fig. 2a). This lifetime is in good
105 agreement with the predicted value of $44(6)$ s based on the measured ground-state trap
106 lifetime of $96(8)$ s, and the expected contributions from trap induced Raman scattering and
107 black-body radiation [28, 31].

108 Our measured lifetimes suggest that at $15E_R$, the Ramsey contrast should decay expo-
109 nentially with a time constant of $55(8)$ s. In practice, this decay is exacerbated by tweezer-
110 induced frequency shifts associated with slight variations in the trapping wavelength be-
111 tween tweezers [23, 24]. The result is Gaussian decay with an expected time constant of
112 $33(1)$ s [30, 32]. In our measurements, the signal at each Ramsey time is a single-shot mea-
113 surement such that even though atom-laser coherence decays over ~ 3 s [30], we can infer
114 the atomic coherence from the variance of this signal, which remains high on much longer
115 timescales (Fig. 2b) [30]. The atomic coherence, and thus Ramsey contrast, inferred from
116 this measurement decays with a $1/e$ time of $19.5(8)$ s (Fig. 2b), slightly faster than the
117 prediction based on the measured lifetime and dephasing. This corresponds to an effective
118 quality factor of $Q = 1.9(1) \times 10^{16}$, which is limited by inhomogeneous broadening.

Even in the absence of atom-laser coherence, we can perform a synchronous clock comparison that takes advantage of this long-lived atomic coherence by comparing the relative phase between two sub-ensembles in the tweezer array [23, 33, 34]. Because readout occurs in a site-resolved manner, the partitioning of these ensembles can be chosen arbitrarily. Specifically, we choose a “checkerboard” partitioning that yields no net tweezer-induced frequency shift between the two sub-ensembles, and a “diagonal” partitioning that yields a near-maximal frequency shift (Fig. 3a insets). At Ramsey dark times that exceed the atom-laser coherence time, the Ramsey phase is randomized. As a result, parametric plots of the excitation fraction in the two sub-ensembles result in points that randomly fall along the edge of an ellipse, where the size of the ellipse is related to the average atomic coherence, and the opening angle of the ellipse is related to the net phase (and thus frequency) shift between sub-ensembles (Fig. 3a). Extracting a phase from these distributions via ellipse fitting, particularly in the presence of QPN, yields biased results near zero phase or contrast [34, 35]. While this means that any useful measurement must operate away from this point, to initially identify an optimal Ramsey time with respect to relative stability we choose to operate in a biased regime with no phase offset. This is because any partitioning that yields a frequency shift results in a phase offset, and thus bias, that varies with Ramsey time, obscuring the optimal value. We characterize this biasing via Monte-Carlo simulations [32] which, when combined with the expected effects of QPN, are in good agreement with the data (Fig. 3b).

Guided by these measurements, we perform a 4.3 hour-long synchronous comparison between sub-ensembles at the near-optimal Ramsey time of 15 s. At 15 s, the diagonal partitioning results in a sufficiently large tweezer-induced phase shift between sub-ensembles to eliminate the effects of biasing (Fig. 3b, c). This is confirmed both via the same Monte-Carlo simulations used above to characterize bias, and by the agreement between the data and a prediction based exclusively on QPN. Specifically, we expect a tweezer-induced frequency offset of $7.0(1.3)$ mHz based on previous measurements of the light shift [24, 36], and measure an offset of $7.15(18)$ mHz. The uncertainty in this measurement corresponds to a fractional frequency precision of 4.2×10^{-19} . In this unbiased condition, we compute the Allan deviation [32], which averages down with a slope of $5.2(3) \times 10^{-17} (\tau/s)^{-1/2}$. This is in good agreement with the expected value of $5.2 \times 10^{-17} (\tau/s)^{-1/2}$ from QPN with no bias correction (Fig. 3c), and comparable to the state of the art value of $3.1 \times 10^{-17} (\tau/s)^{-1/2}$.

151 for such synchronous comparisons reported in leading 3D lattice clocks [7]. Moreover, the
152 long interrogation times used here allow us to match the highest duty cycles achieved in
153 our previous work of 96% [24], even without performing repeated interrogation. As a result,
154 while not demonstrated here, Dick effect noise is not expected to significantly impact the
155 stability of an asynchronous comparison [24].

156 To better understand the limitations of this system, we study atomic coherence within
157 the array using the single-site observables afforded by our microscope, and look for classical
158 correlations in the states of the atoms after Ramsey evolution. Specifically, we compute
159 the $g^{(2)}$ correlator [32] between atoms in different tweezers as a function of Ramsey dark
160 time and relative tweezer position $\Delta\vec{r}$, which we denote as $C(\Delta\vec{r})$ (Fig. 4a) [37–39]. After
161 averaging over the phase of the laser, for two atoms 1 and 2 each with density matrix $\rho_{j=1,2}$,
162 the correlator is equal to $2A_1A_2 \cos(\phi_1 - \phi_2)$ where $\rho_{eg,j} = A_j e^{i\phi_j}$. This quantity serves as
163 a site-resolved measure of tweezer-induced clock transition shifts [32, 37–39], revealing that
164 along the forward diagonal of the array, where frequency offsets between tweezers — and
165 thus clock frequency offsets — are maximal, the atoms become uncorrelated, and eventually
166 develop negative correlations. Along the anti-diagonal, where there is no frequency offset
167 between tweezers, positive correlations persist over much longer timescales. We further
168 observe the development of fringes in the correlator along the more tightly spaced axis of
169 the array, which we hypothesize are the result of overlaps between tweezers [32].

170 The coherence of a given atom, $|\rho_{eg}|$, may be defined with respect to a partner atom,
171 or an ensemble of atoms, which serves as a phase reference [34, 38, 40]. If the atom and
172 reference are at the same frequency, any excess decay of correlations between the atom
173 and reference compared to the decay of the reference can be attributed to loss of single-
174 atom coherence [32]; if the frequencies are different, the signal falls more rapidly due to
175 the evolving phase difference and constitutes a lower bound on the single-atom coherence
176 time. Hence, we can compare the average correlations between one atom and the total
177 spin projection of the remaining array, C_A , with the measured Ramsey contrast (Fig. 4b).
178 Applying this procedure to the atoms in the central 4×4 sites, which have a clock frequency
179 similar to that of the array mean, we infer a single-atom $1/e$ coherence time of $48(8)$ s and a
180 resulting atomic oscillator quality factor of $Q = 6.5(1.1) \times 10^{16}$ (Fig. 4c). This is comparable
181 to the expected value of $55(8)$ s, and corresponds to the useable timescale for frequency
182 comparison measurements (as in Fig. 3) that we would expect if all tweezers were at the

183 same wavelength, as might be achieved with the use of a spatial light modulator.

184 In order to extend this argument to each atom in the array, particularly to those whose
185 clock frequencies differ substantially from the ensemble mean, we can simply choose a phase
186 reference that has a similar frequency to the atom under measurement. Specifically, we con-
187 sider 2×2 sub-ensembles of the array, for which we expect tweezer-induced dephasing to be
188 suppressed to a timescale of several hundred seconds. In this case, the sub-ensemble-averaged
189 single-atom coherence can be written in terms of the average of the pairwise correlators [32].
190 With reasonable assumptions [32], the square root of this quantity averaged across all such
191 sub-ensembles contained in the array, $\sqrt{C_{2 \times 2}}$, provides a lower bound on the average atomic
192 coherence $|\bar{\rho}_{eg}|$ of all ~ 150 atoms in the array. This bound has a measured $1/e$ lifetime of
193 33(2) s (Fig. 4c).

194 These coherence times and atom numbers have advanced the state of the art in atomic
195 coherence at optical frequencies, and pushed tweezer clocks to a new regime of relative
196 stability. This is accomplished via a new recipe for creating tailored optical potentials that
197 results in a substantial increase in accessible sample sizes to hundreds of tweezers in this
198 work, and presents a clear path towards scaling to more than a thousand tweezers [30, 32].

199 The advances in this work are, in part, guided by ground-breaking studies in optical lattice
200 clocks [28], and might also illuminate new paths forward for these lattice systems that benefit
201 from greater atom number than tweezer clocks. While the elimination of tunneling in this
202 work is partially due to increased trap separation in comparison to lattice clocks, a far greater
203 effect is the presence of disorder. Specifically, as is well-known in tweezer systems [41, 42],
204 tweezer-to-tweezer disorder is hard to suppress on the energy scale of the tunneling. While
205 this is a challenge for their use in Hubbard physics, here it serves to suppress tunneling
206 and prolong atomic coherence. This suggests that, in the context of lattice clocks, the
207 use of a weak disordering potential super-imposed on a standard optical lattice clock could
208 enhance coherence time, which might be an alternative solution to directly modulating the
209 tunneling [28]. This highlights another important role for the tweezer clock: it serves as a
210 clean, versatile platform for studying neutral-atom optical clocks and the mechanisms that
211 influence their performance. In future accuracy studies [30], the lack of interactions and
212 itinerance in this system will ease dissection of coupled systematic effects.

213 Our work here lays a firm foundation for engineering entanglement on an optical clock
214 transition [9, 43]. The large 2D arrays and tight spacings used in this work are key for fu-

ture studies involving limited-range Rydberg interactions, providing access to larger samples with higher connectivity, stronger interactions, and correspondingly greater entanglement. Furthermore, incremental upgrades to our existing setup [30, 32] will improve purity in state preparation by reducing imaging losses [4, 5, 24, 44] and allowing for higher fidelity clock rotations, which will be key to implementing protocols for generating entanglement [9, 18, 45]. While many-body entanglement scales exponentially poorly with single-particle decoherence, the coherence times reported here establish the prospect of a metrologically useful entangled optical clock operating with tens of atoms and seconds-long interrogation times. Our use of ^{88}Sr , whose clock linewidth is tunable with a magnetic field, also establishes longer-term directions for quantum metrology that are not fundamentally limited by spontaneous emission [46]. The microscopic control available in this system further opens the possibility of probing and verifying entanglement with microscopic observables, and, in the context of quantum simulation, implementing various 2D spin models of interest [47–49]. For applications in quantum information, such a system can also be used to perform Rydberg-mediated quantum gates on long-lived spin or optical qubits [16, 17, 21], or to prepare cluster states in a highly parallelized way for use in measurement-based quantum computing [50].

FIG. 1. 3D ground-state cooled strontium atoms in a 320-site clock-magic wavelength tweezer array. a) In order to generate large numbers of traps that are compatible with ground-state cooling and narrow-line spectroscopy, we combine a shallow clock-magic “science” potential at 813 nm with a tightly confining “auxiliary” potential at 515 nm, which includes both a tweezer array and a crossed-beam optical lattice to provide tight confinement along all spatial axes. b) Representative single shot (top) and averaged (bottom) images of atoms demonstrate site-resolved readout of the 16×20 array of tweezers used in this work, with a spacing of $1.2 \mu\text{m}$ ($1.5 \mu\text{m}$) in the vertical (horizontal) direction. The red circles in the single-shot image denote the tweezer positions to guide the eye. c) In a typical experimental sequence these potentials cooperate to prepare and readout 3D ground-state cooled atoms in traps that are compatible with narrow-line clock spectroscopy. d) To confirm that the atoms in the science potential are appropriately cooled, we perform sideband spectroscopy after cooling in the auxiliary potential (black points), and after adiabatically transferring the atoms to and back from the science potential (grey points, see main text for detail). Cartoons in the top left of each frame indicate the orientation of the probe beam relative to the traps, showing probes in the radial direction (left) and in the axial direction (right). e) With atoms trapped in the science potential, array-averaged Rabi spectroscopy of the $^1\text{S}_0 \leftrightarrow ^3\text{P}_0$ clock transition provides Fourier-limited linewidths of $10.1(2)$ Hz and $0.62(1)$ Hz (full width at half maximum), in good agreement with the expected sinc lineshapes based on the known probe durations used in each case (solid lines). Callout (top) shows the Fourier-limited 0.6 Hz feature in detail, with no reduction in maximal transfer fraction compared to the 10 Hz case. Error bars are smaller than the point size. We investigate the presence of inhomogeneous, trap-dependent shifts of the clock transition by independently fitting the centers of the spectra associated with each tweezer, which vary with a standard deviation of $0.039(2)$ Hz (right).

FIG. 2. Minute-scale atomic lifetime and ensemble coherence studies. a) To determine limits on atomic coherence, we measure the lifetime of both the ground (${}^1\text{S}_0$, black points) and clock (${}^3\text{P}_0$, black circles) states. For ground-state atoms the lifetime saturates to 160(10) seconds in deep traps, with additional technical sources of atom loss contributing in shallower traps (exponential fit to ${}^1\text{S}_0$ data, dark grey). For clock-state atoms an optimal trap depth arises from a competition between this atom loss, which prefers deep traps, and depumping via spontaneous Raman scattering of the trap light (theory prediction with no free parameters, light grey) [28, 30, 31], which prefers shallow traps. The combination of these loss mechanisms (dashed line) is in good agreement with the measured clock-state lifetimes, including the optimum of 46(5) seconds at 14E_R . b) For clock operation, we perform Ramsey spectroscopy in 15E_R deep tweezers (black points), near this optimal depth. Given the measured clock-state lifetime, we would expect the contrast to decay with an exponential time constant of 55(8) s (light-grey region). However, we expect tweezer-dependent light shifts to result in Gaussian decay with a time constant of 33(1) s at 15E_R [24, 30, 32]. The combination of these two effects is denoted by the medium-grey region. Note that each data point corresponds to a single shot of the experiment. As a result, despite the fact that the atom-laser coherence decays over 3.6(2) s (dark-grey region)[30], the variance of the Ramsey signal decays on a timescale set by atomic coherence. This is clarified by the insets, which share units with the main axes, and show detailed views of Ramsey evolution at a few different times. Here, it is possible to see the initial loss of phase coherence with the laser followed, at later times, by total loss of coherence (and thus variance in this signal) in the system.

FIG. 3. Resolving millihertz shifts of an optical transition. a) We perform a synchronous clock comparison by partitioning the array into two sub-ensembles (insets, red and blue), and creating a parametric plot of the 3P_0 excited-state fraction in the blue ensemble (P_b) vs in the red ensemble (P_r) (in this case at a 15 s interrogation time in $15E_R$ deep tweezers). In the checkerboard (left) partitioning there is no mean frequency shift between the two sub-ensembles, whereas in the diagonal (right) case we expect a 7.0(1.3) mHz shift [30, 32]. The relative frequency between the sub-ensembles can be extracted via ellipse fitting (red lines), which in the diagonal case yields 7.15(18) mHz. Note that such fits are biased near zero phase shift, as is evident in the fit to the checkerboard ensemble, which returns an artificially large phase shift. b) To identify an optimal Ramsey dark time, we compute the fractional frequency uncertainty between the sub-ensembles as a function of Ramsey time at fixed total averaging time [32]. The black points (grey point) correspond(s) to 13 minutes (4.3 hours) of averaging, and are extracted from the checkerboard partitioning. Note that these values are not representative of a true stability due to biasing. This is made clear by the dashed curves, which correspond to expected QPN, and the solid grey curves, which include an additional correction factor calculated via Monte-Carlo simulations to account for the biased fits (shaded regions denote 1-sigma confidence interval) [32]. At 15 s interrogation times the diagonally separated sub-ensembles have a sufficient phase shift to remove the bias in the fits. This condition (red star) shows the fractional frequency uncertainty of the full 4.3 hour-long measurement, with a value of 4.2×10^{-19} . This is in good agreement with the expected QPN limit with no bias correction (red curve). c) We can further compute an Allan deviation associated with this measurement (black points), which averages down with a slope of $5.2(3) \times 10^{-17} (\tau/s)^{-1/2}$ (black dashed line). This is in good agreement with the expected value of $5.2 \times 10^{-17} (\tau/s)^{-1/2}$ from QPN (red line). Red star is duplicated here as a point of comparison (note that this point is not strictly an Allan deviation, and is extracted via jackknifing) [32].

FIG. 4. Microscopic studies of atomic coherence. a) As a measure of atomic coherence we compute the spatially resolved atom-atom correlation function, $C(\Delta\vec{r})$ [32], as a function of Ramsey dark time. These plots are normalized by $C_{2\times 2}$, as defined below, to isolate the effects of dephasing from atom loss and decay. The relative displacements $\Delta r_{x,y}$ are normalized by the array spacing in the relevant direction ($a_x = 1.5 \mu\text{m}$, $a_y = 1.2 \mu\text{m}$) such that the pixel spacing corresponds to the tweezer spacing. Solid (dashed) diagonal lines indicate axes along which the tweezer wavelengths change (remain constant) showing accelerated (reduced) dephasing along the forward (reverse) diagonal of the array due to tweezer-induced frequency shifts (solid contour shows where the correlator passes through zero). The fourth frame is a theoretical prediction at 25 s given our known tweezer frequencies and depths. b) The coherence of a single atom (red circle in cartoon) can be measured by computing the average correlations C_A between it and an ensemble of reference atoms (blue circles). In this case the reference ensemble is the entire array, and the excess decay of C_A (red points, averaged over a 4×4 block of atoms at the center of the array) compared to the decay of the Ramsey contrast (black points) can be used to quantify the single-atom coherence time. Fits to these quantities (dashed lines) with a Gaussian and exponential component yield overall $1/e$ times of 14.6(7) s and 19.5(8) s respectively. c) Based on these measurements, we can infer a single-atom coherence time of 48(8) s (dashed line) [32], which is in good agreement with a model based on the measured lifetimes and initial Ramsey contrast (solid line, error in grey). Open circles are C_A with the decay associated with the reference ensemble divided out, which serves as a direct measurement of the single-atom coherence $|\rho_{eg}|$. In the absence of dephasing, an ensemble of these atoms would have a Ramsey contrast of $2|\rho_{eg}|$ [32]. To extend this measurement from the central 4×4 region to the full array, we consider the average correlation between all atom pairs in a 2×2 block averaged over all such blocks, $C_{2\times 2}$. In this case each atom in the block acts as a reference for all other atoms in the block (see cartoon). The square root of this quantity (black squares) decays with a fitted $1/e$ time of 33(2) s (double-dashed line), and serves as a lower bound on the average atomic coherence across the entire array [32].

231 * E-mail: adam.kaufman@colorado.edu

- 232 [1] Ludlow, A. D., Boyd, M. M., Ye, J., Peik, E. & Schmidt, P. O. Optical atomic clocks. *Rev.*
233 *Mod. Phys.* **87**, 637–701 (2015).
- 234 [2] Georgescu, I. M., Ashhab, S. & Nori, F. Quantum simulation. *Rev. Mod. Phys.* **86**, 153–185
235 (2014).
- 236 [3] Preskill, J. Quantum computing and the entanglement frontier. *ArXiv12035813 Cond-Mat*
237 *Physicsquant-Ph* (2012).
- 238 [4] Cooper, A. *et al.* Alkaline-earth atoms in optical tweezers. *Phys. Rev. X* **8**, 041055 (2018).
- 239 [5] Norcia, M. A., Young, A. W. & Kaufman, A. M. Microscopic control and detection of ultracold
240 strontium in optical-tweezer arrays. *Phys. Rev. X* **8**, 041054 (2018).
- 241 [6] Saskin, S., Wilson, J. T., Grinkemeyer, B. & Thompson, J. D. Narrow-line cooling and imaging
242 of ytterbium atoms in an optical tweezer array. *Phys. Rev. Lett.* **122**, 143002 (2019).
- 243 [7] Campbell, S. L. *et al.* A Fermi-degenerate three-dimensional optical lattice clock. *Science*
244 **358**, 90–94 (2017).
- 245 [8] Oelker, E. *et al.* Demonstration of 4.8×10^{-17} stability at 1 s for two independent optical
246 clocks. *Nature Photonics* **13**, 714–719 (2019).
- 247 [9] Gil, L. I. R., Mukherjee, R., Bridge, E. M., Jones, M. P. A. & Pohl, T. Spin squeezing in a
248 Rydberg lattice clock. *Phys Rev Lett* **112**, 103601 (2014).
- 249 [10] Saffman, M., Walker, T. G. & Molmer, K. Quantum information with Rydberg atoms. *Rev.*
250 *Mod. Phys.* **82**, 2313–2363 (2010).
- 251 [11] Browaeys, A. & Lahaye, T. Many-body physics with individually controlled Rydberg atoms.
252 *Nature Physics* **16**, 132–142 (2020).
- 253 [12] Barredo, D., de Léséleuc, S., Lienhard, V., Lahaye, T. & Browaeys, A. An atom-by-atom
254 assembler of defect-free arbitrary 2d atomic arrays. *Science* **354**, 1021–1023 (2016).
- 255 [13] Endres, M. *et al.* Atom-by-atom assembly of defect-free one-dimensional cold atom arrays.
256 *Science* **354**, 1024–1027 (2016).
- 257 [14] Kumar, A., Wu, T.-Y., Giraldo, F. & Weiss, D. S. Sorting ultracold atoms in a three-
258 dimensional optical lattice in a realization of Maxwell’s demon. *Nature* **561**, 83–87 (2018).
- 259 [15] Brown, M. O., Thiele, T., Kiehl, C., Hsu, T.-W. & Regal, C. A. Gray-molasses optical-tweezer

- loading: Controlling collisions for scaling atom-array assembly. *Phys. Rev. X* **9**, 011057 (2019).
- [16] Levine, H. *et al.* Parallel implementation of high-fidelity multiqubit gates with neutral atoms. *Phys. Rev. Lett.* **123**, 170503 (2019).
- [17] Graham, T. M. *et al.* Rydberg-mediated entanglement in a two-dimensional neutral atom qubit array. *Phys. Rev. Lett.* **123**, 230501 (2019).
- [18] Omran, A. *et al.* Generation and manipulation of Schrödinger cat states in Rydberg atom arrays. *Science* **365**, 570–574 (2019).
- [19] Bernien, H. *et al.* Probing many-body dynamics on a 51-atom quantum simulator. *Nature* **551**, 579–584 (2017).
- [20] de Léséleuc, S. *et al.* Observation of a symmetry-protected topological phase of interacting bosons with Rydberg atoms. *Science* **365**, 775–780 (2019).
- [21] Madjarov, I. S. *et al.* High-fidelity control, detection, and entanglement of alkaline-earth Rydberg atoms. *ArXiv200104455 Cond-Mat Physicsphysics Physicsquant-Ph* (2020).
- [22] Wilson, J. *et al.* Trapped arrays of alkaline earth Rydberg atoms in optical tweezers. *ArXiv191208754 Phys. Physicsquant-Ph* (2019).
- [23] Madjarov, I. S. *et al.* An atomic-array optical clock with single-atom readout. *Phys. Rev. X* **9**, 041052 (2019).
- [24] Norcia, M. A. *et al.* Seconds-scale coherence on an optical clock transition in a tweezer array. *Science* **366**, 93–97 (2019).
- [25] Chou, C. W., Hume, D. B., Koelemeij, J. C. J., Wineland, D. J. & Rosenband, T. Frequency comparison of two high-accuracy Al^+ optical clocks. *Phys. Rev. Lett.* **104**, 070802 (2010).
- [26] Brewer, S. M. *et al.* $^{27}\text{Al}^+$ quantum-logic clock with a systematic uncertainty below 10^{-18} . *Phys. Rev. Lett.* **123**, 033201 (2019).
- [27] Ushijima, I., Takamoto, M., Das, M., Ohkubo, T. & Katori, H. Cryogenic optical lattice clocks. *Nat. Photonics* **9**, 185–189 (2015).
- [28] Hutson, R. B., Goban, A., Marti, G. E. & Ye, J. Engineering quantum states of matter for atomic clocks in shallow optical lattices. *Phys. Rev. Lett.* **123**, 123401 (2019).
- [29] Liu, L. R. *et al.* Molecular assembly of ground-state cooled single atoms. *Phys. Rev. X* **9**, 021039 (2019).
- [30] See methods and extended data.
- [31] Dörscher, S. *et al.* Lattice-induced photon scattering in an optical lattice clock. *Phys. Rev. A*

- 291 **97**, 063419 (2018).
- 292 [32] See supplemental materials.
- 293 [33] Takamoto, M., Takano, T. & Katori, H. Frequency comparison of optical lattice clocks beyond
294 the Dick limit. *Nature Photon* **5**, 288–292 (2011).
- 295 [34] Marti, G. E. *et al.* Imaging optical frequencies with $100\mu\text{Hz}$ precision and $1.1\mu\text{m}$ resolution.
296 *Phys. Rev. Lett.* **120**, 103201 (2018).
- 297 [35] Foster, G. T., Fixler, J. B., McGuirk, J. M. & Kasevich, M. A. Method of phase extraction
298 between coupled atom interferometers using ellipse-specific fitting. *Opt. Lett.* **27**, 951 (2002).
- 299 [36] Shi, C. *et al.* Polarizabilities of the ^{87}Sr clock transition. *Phys. Rev. A* **92**, 012516 (2015).
- 300 [37] Chwalla, M. *et al.* Precision spectroscopy with two correlated atoms. *Appl. Phys. B* **89**,
301 483–488 (2007).
- 302 [38] Chou, C. W., Hume, D. B., Thorpe, M. J., Wineland, D. J. & Rosenband, T. Quantum
303 coherence between two atoms beyond $Q = 10^{15}$. *Phys. Rev. Lett.* **106**, 160801 (2011).
- 304 [39] Hume, D. B. & Leibrandt, D. R. Probing beyond the laser coherence time in optical clock
305 comparisons. *Phys. Rev. A* **93**, 032138 (2016).
- 306 [40] Tan, T. R. *et al.* Suppressing Inhomogeneous Broadening in a Lutetium Multi-ion Optical
307 Clock. *Phys. Rev. Lett.* **123**, 063201 (2019).
- 308 [41] Kaufman, A. M. *et al.* Two-particle quantum interference in tunnel-coupled optical tweezers.
309 *Science* **345**, 306–309 (2014).
- 310 [42] Murmann, S. *et al.* Two fermions in a double well: Exploring a fundamental building block
311 of the Hubbard model. *Phys. Rev. Lett.* **114**, 080402 (2015).
- 312 [43] Pedrozo-Peña, E. *et al.* Entanglement-Enhanced Optical Atomic Clock. *ArXiv200607501*
313 *Phys. Physicsquant-Ph* (2020).
- 314 [44] Covey, J. P., Madjarov, I. S., Cooper, A. & Endres, M. 2000-times repeated imaging of
315 strontium atoms in clock-magic tweezer arrays. *Phys. Rev. Lett.* **122**, 173201 (2019).
- 316 [45] Kaubruegger, R. *et al.* Variational spin-squeezing algorithms on programmable quantum
317 sensors. *Phys. Rev. Lett.* **123**, 260505 (2019).
- 318 [46] Kessler, E. M. *et al.* Heisenberg-limited atom clocks based on entangled qubits. *Phys. Rev.*
319 *Lett.* **112**, 190403 (2014).
- 320 [47] Zhang, G. & Song, Z. Topological characterization of extended quantum Ising models. *Phys.*
321 *Rev. Lett.* **115**, 177204 (2015).

- ³²² [48] Savary, L. & Balents, L. Quantum spin liquids: A review. *Rep. Prog. Phys.* **80**, 016502 (2017).
- ³²³ [49] Titum, P., Iosue, J. T., Garrison, J. R., Gorshkov, A. V. & Gong, Z.-X. Probing ground-state
phase transitions through quench dynamics. *Phys. Rev. Lett.* **123**, 115701 (2019).
- ³²⁴ [50] Briegel, H. J., Browne, D. E., Dür, W., Raussendorf, R. & Van den Nest, M. Measurement-
based quantum computation. *Nat. Phys.* **5**, 19–26 (2009).
- ³²⁵
- ³²⁶

327 **METHODS**

328 **Hybrid potentials**

329 Our science potential is a 2D tweezer array operating at 813 nm, a magic wavelength
330 for the clock transition [24], whereas the auxiliary potential operates at 515 nm, where a
331 magic trapping condition can be achieved for the $^1\text{S}_0 \Leftrightarrow ^3\text{P}_1$ cooling transition at 689 nm
332 via tuning of a magnetic field [5]. The power requirements at 813 nm are more demanding
333 compared to 515 nm, due to the roughly $3 \times$ lower polarizability, larger diffraction-limited
334 spot size, and reduction in available laser power at this wavelength. However, critically,
335 because the science potential is only used for the clock-interrogation stage where shallow
336 traps are preferable, these power constraints do not impose a limitation on atom number or
337 state preparation.

338 The auxiliary potential includes a 2D tweezer array and a crossed-beam optical lattice,
339 which provides additional confinement along the weakly confined “axial” axis of the tweez-
340 ers. Because the required confinement is the same in all axes for 3D ground-state cooling,
341 this axial lattice greatly reduces the power requirements on the auxiliary tweezers. In our
342 apparatus, with a numerical aperture of $\text{NA} \simeq 0.68$, this corresponds to a ~ 30 -fold re-
343 duction in required optical power per tweezer. As a result, at modest optical power, we
344 can create near-spherical traps with roughly 90 kHz trap frequencies in all axes. Including
345 various losses in our system, and using ~ 4 W of total optical power, we create 320 such
346 traps in a 16×20 array (see Fig. 1b, d of main text).

347 While the tweezers, and thus the radial trap frequencies, can be balanced across the entire
348 array, there is substantial inhomogeneous broadening of the axial trap frequencies. This is
349 due to the relatively small 25 μm waists of the lattice beams, which are comparable to the
350 extent of the tweezer array (Fig. E1). As mentioned in the main text, the axial cooling
351 and handoff performance is vastly improved in a 6×6 region at the center of the array,
352 with an average phonon occupation of $\bar{n} = 0.00^{+0.06}_{-0.00}$ ($\bar{n} = 0.06^{+0.10}_{-0.06}$), compared to the array
353 average of $\bar{n} = 0.07^{+0.14}_{-0.07}$ ($\bar{n} = 0.25 \pm 0.12$) before (after) the handoff. Due to the modest
354 power requirements of the lattice, the lattice waist could easily be increased in the future
355 without sacrificing axial trap frequency, suggesting that this enhanced performance could
356 be achieved across the entire array.

357 *Tweezer Arrays*

358 To prepare our 2D tweezer arrays, we image two orthogonal acousto-optic deflectors
359 (AODs) onto each other in a $4f$ configuration. Two such systems at 515 nm and 813 nm are
360 combined on a dichroic and projected via the same high-numerical-aperture objective lens,
361 which has diffraction-limited performance between 461 nm and 950 nm. Relevant 515 nm
362 and 813 nm tweezer parameters are collected in table E1.

363 We space the two axes of our array differently, with 1.5 and 1.2 μm spacings along the
364 two orthogonal axes of the array, corresponding to ~ 5 MHz (~ 3 MHz) offsets between
365 adjacent 515 nm (813 nm) tweezers. This keeps nearby tweezers at different optical fre-
366 quencies, such that any interference is time-averaged away and can be compensated for by
367 trap balancing. For equally spaced tweezers, we have observed DC interference fringes that
368 cannot be removed due to a lack of access to the appropriate degrees of freedom in trap
369 balancing.

370 In order to balance the depths of individual tweezers, we split off a small fraction of the
371 light before the objective, and measure the integrated intensity per tweezer using a CMOS
372 camera. By adjusting the relative power in the different radio frequency (RF) tones applied
373 to the crossed AODs, it is possible to balance the total optical power in each spot to within
374 5% of the mean, as measured on the camera. The main limitation on this balancing is
375 a lack of fully independent control over each spot — each of the $16 + 20 = 36$ RF tones
376 has independent phase and amplitude control, however, the relative phases are more or less
377 fully constrained to avoid large voltage spikes that can cause intermodulation due to non-
378 linearities in the electronics that drive the tweezer system. As a result, we only have 36
379 degrees of freedom for balancing a tweezer array of $16 \times 20 = 320$ spots. While it is possible
380 to explicitly balance the tweezer powers at the atoms (e.g. via light shifts or measurements
381 of the trap frequency), we have not yet found this to be necessary, as the variations in trap
382 depth are currently dominated by this lack of independent control.

383 *Tweezer RF source*

384 To supply the AODs used to generate our tweezers with appropriate RF signals, we use
385 a custom field programmable gate array (FPGA)-based frequency synthesizer. Specifically,

386 the FPGA runs 512 direct digital synthesis (DDS) cores, which are interleaved to generate
387 256 outputs with independently tunable frequency, phase, and amplitude. These outputs
388 control 4 separate 16-bit digital-analogue converters (DACs) which each drive one of the
389 four AODs used in our system. This corresponds to 64 independent RF tones per AOD,
390 where each tone has 36-bits of frequency resolution, 12-bits of phase resolution, and 10-bits
391 of amplitude resolution. The outputs are clocked at 750 MHz (but can be clocked in the
392 gigahertz range if desired), corresponding to a maximum usable frequency of \sim 300 MHz
393 (for this work we operate in the 100-200 MHz range). These outputs are amplified using
394 two stages of linear RF amplifiers, with the final stage being a high power (10 W) amplifier
395 that delivers \sim 2 W (\sim 5 W) of total RF power to each of the 515 nm (813 nm) AODs.

396 *Axial lattice*

397 To form the axial lattice, \sim 300 mW of 515 nm light is split in an interferometer that
398 creates two parallel beams with variable spacing and controllable relative phase. These two
399 beams are focused onto the atoms with a 30 mm achromatic doublet, such that each beam
400 has a Gaussian $1/e^2$ radius of 25 μm at the atoms. These beams interfere to form a standing
401 wave with k-vector normal to the tweezer plane. For the chosen beam spacing of 1.6 cm at
402 the lens, the resulting lattice potential has a period of $\lambda_l \approx 1 \mu\text{m}$. We are able to flatten
403 this potential relative to the tweezer array at the $\lambda_l/10$ level (see Fig. E2) [32].

404 **Experimental procedure**

405 Our procedure for loading, ground-state cooling, and imaging bosonic strontium-88 (^{88}Sr)
406 atoms in 515 nm optical tweezers is described in [5]. Power hungry operations like initial
407 loading and imaging are performed exclusively in these tweezers. We have observed that
408 loading can be performed in even shallower tweezers with the aid of the axial lattice; however,
409 this results in an additional background of atoms that populate other layers of the lattice.
410 To avoid this, we opt to load directly into the tweezers to ensure loading of a single atom
411 plane.

412 In this work, the axial lattice is used primarily for improved sideband cooling [4, 5, 51–
413 53] in the axial direction. It is ramped on and off over 5 ms, and is shuttered for all stages

414 of the experiment except for when performing sideband cooling. To shrink the size of the
415 atomic wave packet and prevent loading of adjacent lattice fringes, we perform 5 ms of un-
416 resolved axial and resolved radial sideband cooling in the tweezers before ramping on the
417 axial lattice. The improved axial confinement with the lattice on creates nearly isotropic
418 traps with \sim 90 kHz trap frequencies along all axes, and further cooling in this hybrid
419 potential brings most of the atoms ($81^{+17}_{-22}\%$) to the 3D motional ground state. Since the
420 polarization of the axial lattice is aligned to that of the 515 nm tweezers, we maintain the
421 same “magic field” conditions throughout this sequence [5].

422 To hand atoms between the two sets of tweezers, we ramp on the 813 nm tweezers in
423 5 ms with the 515 nm tweezers maintained at full depth, and then ramp the 515 nm tweezers
424 off. The intensity servo for our 515 nm tweezers takes a few milliseconds to stabilize after
425 being turned back on, which can heat atoms out of the 813 nm tweezers. To avoid this,
426 while the 515 nm tweezers are nominally switched off we also move them away from the
427 atoms with the AODs used to project them, and then shutter the 515 nm beam path. To
428 reintroduce the 515 nm tweezers, we turn on the beam and let the intensity servo settle to
429 low power, un-shutter the beam path, and finally move the tweezers back to overlap with
430 the 813 nm array. By shuttering the beam, we ensure that there are no light shifts of the
431 clock transition due to stray 515 nm light while the atoms are in the 813 nm tweezers. Note
432 that while the handoff procedure can be performed with 0.0(3)% atom loss, for all clock
433 data in the main text this alignment was imperfect, resulting in an additional $\sim 4\%$ atom
434 loss when handing atoms to and back from the science potential. In this work, we choose
435 not to correct this loss because it is inconsequential for clock performance, however, more
436 careful and consistent calibration will be necessary for future works that are more sensitive
437 to state purity.

438 *Clock interrogation*

439 After loading ground-state cooled atoms into the science potential, we can interrogate
440 the clock transition. As in our previous work [24], we apply a magnetic field of 22 G to mix
441 the 3P_1 state into the 3P_0 state which opens the doubly forbidden $^1S_0 \leftrightarrow ^3P_0$ transition at
442 698 nm [54], at which point this transition can be driven optically. To avoid fluctuations
443 in clock Rabi frequency due to intensity fluctuations, we opt to ramp up the clock laser

⁴⁴⁴ intensity with the laser detuned from resonance by 125 kHz. Once the laser intensity servo
⁴⁴⁵ settles, we can jump the detuning to near resonance for a variable time to excite atoms
⁴⁴⁶ to the 3P_0 state. To detect the population excited to 3P_0 we apply a “blow-away” pulse
⁴⁴⁷ of 461 nm light resonant with the ${}^1S_0 \Leftrightarrow {}^1P_1$ transition to remove atoms that were in the
⁴⁴⁸ ground state. To return clock-state atoms to the ground state for readout, we drive the
⁴⁴⁹ ${}^3P_0 \Leftrightarrow {}^3S_1$ transition at 679 nm and the ${}^3P_2 \Leftrightarrow {}^3S_1$ transition at 707 nm (see repumping
⁴⁵⁰ section for additional details). The 3S_1 state decays to the whole 3P_J manifold, such that
⁴⁵¹ eventually all clock-state atoms are pumped into the shorter-lived 3P_1 state and decay back
⁴⁵² to the ground state, where they can be read out during imaging. With this protocol we
⁴⁵³ observe no reduction in 3P_0 maximal transfer fraction when using Rabi frequencies between
⁴⁵⁴ $2\pi \times 7$ Hz and $2\pi \times 0.4$ Hz averaged across all ~ 150 atoms in the array (Fig. 1e).

⁴⁵⁵ All Rabi spectroscopy is performed in $25E_R$ deep tweezers, corresponding to $58 \mu\text{W}$ of op-
⁴⁵⁶ tical power per tweezer as measured at the atoms. These shallow traps are the primary limit
⁴⁵⁷ on achievable transfer fraction for all Rabi frequencies used in this work. Specifically, these
⁴⁵⁸ depths result in a relatively high Lamb-Dicke parameter of $\eta = 0.83$, and thus increased
⁴⁵⁹ sensitivity to residual motional excitation [32]. However, the benefit of using such shallow
⁴⁶⁰ traps is that clock frequency shifts arising from spatial variation of the tweezer wavelengths
⁴⁶¹ should be bounded to below 50 mHz across the entire array, resulting in reduced dephas-
⁴⁶² ing [24]. To confirm this, we fit the spectrum of each tweezer to extract its center value,
⁴⁶³ and measure a standard deviation in these trap-dependent clock frequencies of $39(2)$ mHz
⁴⁶⁴ (Fig. 1e).

⁴⁶⁵ For Ramsey spectroscopy, we use a $\pi/2$ -pulse time of ~ 50 ms for all relevant data in
⁴⁶⁶ this paper. At short times, the frequency of the Ramsey fringes is set by the differential
⁴⁶⁷ light-shift imposed by the probe beam on the 1S_0 and 3P_0 states. At longer times, the loss
⁴⁶⁸ of atom-laser coherence manifests as a randomised phase of the second $\pi/2$ pulse in the
⁴⁶⁹ Ramsey sequence. This obscures Ramsey oscillations but preserves the probability of large
⁴⁷⁰ excursions due to the persistence of atomic coherence, where atomic coherence is defined
⁴⁷¹ as the magnitude of the off-diagonal elements in the average single-particle density matrix,
⁴⁷² $|\rho_{eg}|$.

473 *Repumping*

474 Our clock-state lifetime measurements can be confounded by the presence of atoms
475 pumped into the 3P_2 state due to Raman scattering of the trap light. These atoms are
476 not distinguished from clock-state atoms during our normal blow-away measurement, and
477 can lead to an artificially long inferred lifetime. To avoid this, we add an additional repump-
478 ing step that depletes 3P_2 atoms before the blow-away by driving the ${}^3P_2 \leftrightarrow {}^3S_1$ transition at
479 707 nm. Note that since 3S_1 decays to 3P_0 with a branching ratio of $\sim 1/9$, this measurement
480 alone is insufficient to accurately determine the population in 3P_0 . As a result, we repeat the
481 above measurement without repumping to measure the total ${}^3P_0 + {}^3P_2$ population. Based
482 on these two measurements we infer the true population in 3P_0 , which appears in Fig. 2a.

483 **Trap lifetime**

484 *Deep traps*

485 We expect our trap lifetimes, particularly in deeper traps, to be limited by collisions with
486 residual background gas. These collisions are substantially more energetic than the trap
487 depths we have access to, resulting in a vacuum lifetime that is effectively independent of
488 trap depth [55]. This is confirmed via the procedure in [56], assuming that the main collision
489 partners are room temperature Σ state H₂ molecules interacting via Van der Waals forces.

490 Based on this model, we expect clock-state atoms to have reduced trap lifetimes τ com-
491 pared to ground-state atoms due to their larger C_6 coefficient and thus larger scattering cross
492 section σ , since in this case $\tau \propto 1/\sigma \propto C_6^{-2/5}$. With the known C_6 coefficients for collisions
493 between H₂ and ⁸⁸Sr [57] we calculate that the ratio between the ground and clock-state
494 trap lifetime (τ_g and τ_e respectively) is $\tau_g/\tau_e = 1.10$, which agrees with results from [31].

495 We estimate that the fractional frequency shifts due to these background collisions [58, 59]
496 are below the 10^{-19} level, suggesting that this is not a likely explanation for the increased
497 decoherence rate observed in the main text.

499 The source of the dramatic reduction of trap lifetime in shallow traps is as of yet unknown;
 500 however, based on the above analysis we rule out the effect of collisions with background
 501 gas. Other potential sources could include tunneling, or heating induced by parametric
 502 modulation, pointing noise, or scattered light.

503 For $6E_R$ deep tweezers with $1.2 \mu\text{m}$ spacing, we calculate a tunneling rate of $\sim 1 \text{ Hz}$
 504 between adjacent tweezers via exact diagonalization in 1D. For image pairs in the experi-
 505 ment, we expect this tunneling to manifest as correlated nearest-neighbor atom-vacancy and
 506 vacancy-atom events, where an atom tunnels from one site to an empty adjacent site, or
 507 pairs of atom-vacancy events, where an atom tunnels onto an occupied adjacent site, and
 508 both atoms are lost due to light-assisted collisions. We do not observe an excess of such
 509 events beyond what is expected due to loss and imaging infidelity at any depth or hold time
 510 used in this work. This suggests that disorder, which we know is present on the scale of
 511 $> 10^{-2}$ in trap depth, plays a critical role in pinning the atoms. Given the relevant tunneling
 512 energies this is not unexpected, since even in our shallowest traps disorder on the scale of
 513 10^{-4} in trap depth is sufficient to freeze out tunneling. Similar calculations suggest that the
 514 effect of loss due to Zener tunneling along the gravitational axis is negligible at all depths
 515 explored in this work.

516 Atom loss can also arise from heating caused by a variety of mechanisms including inten-
 517 sity and pointing noise from the trap laser, and scattered light. Intensity noise manifests as
 518 parametric modulation of the trap frequency which, assuming a flat noise spectrum, results
 519 in exponential heating (measured in phonon number) with a time constant proportional to
 520 f_t^2 , where f_t is the trap frequency. Similarly, pointing noise with a flat spectrum results in
 521 linear heating with a rate proportional to f_t^3 [60, 61]. For comparison, the number of bound
 522 states, N , in a tweezer scales roughly like $N \propto \sqrt{U} \propto f_t$, where U is the trap depth. As
 523 such, assuming a flat noise spectrum, both these sources of loss should improve with reduced
 524 trap depth.

525 While the intensity noise of our trapping laser is suppressed below 10 kHz via a servo,
 526 and otherwise relatively flat over the frequencies relevant for heating, we do not expect this
 527 to be true for pointing noise. In this case there is increased noise at lower frequencies due
 528 to mechanical resonances and acoustic noise, and no convenient way of removing such noise

529 with a servo. As a result pointing noise likely contributes to our reduced lifetimes at and
530 below trap depths of $15E_R$ (corresponding to 6.8 kHz trap frequencies). Other sources of
531 trap-independent heating, like scattered background light, can also begin to dominate as the
532 traps become very shallow and N becomes small.

533 **Clock-state lifetime and coherence**

534 The 3P_0 clock-state lifetime is primarily limited by the loss processes described above,
535 as well as by scattering of black-body radiation and the trapping light. Because we di-
536 rectly measure the 3P_0 population in the main text, we are sensitive to all processes that
537 remove population from this state, including transitions to the metastable 3P_2 state. Ra-
538 man scattering of the trap light can drive such transitions, with dominant contributions
539 from $^3P_0 \rightarrow ^3P_1$ and $^3P_0 \rightarrow ^3P_2$. For π -polarized trap light, these processes occur with
540 rates of $4.98 \times 10^{-4} s^{-1} E_R^{-1}$ and $2.84 \times 10^{-4} s^{-1} E_R^{-1}$ respectively [31]. Note that while the
541 ratio of these two scattering processes is polarization-dependent, their sum, with a value of
542 $\Gamma_{12}^R = 7.82 \times 10^{-4} s^{-1} E_R^{-1}$, is conserved. All population driven into 3P_1 can be assumed to
543 immediately decay into the ground state, whereas processes that return population in 3P_2
544 to the 3P_0 state are negligible. As such, to a good approximation, Γ_{12}^R can be treated as the
545 total rate at which population in 3P_0 is depleted due to Raman scattering.

546 Black-body radiation can off-resonantly drive transitions to the 3D_1 state, which decays
547 to the 3P_J manifold with branching ratios of $R_J^D = 59.65\%$, 38.52% , and 1.82% for the
548 $J = 0, 1$ and 2 states respectively [31]. The dominant mechanism by which black-body
549 radiation contributes to decay of the 3P_0 state is via population that branches from 3D_1
550 into 3P_1 , and subsequently decays into the ground state. This process occurs at a rate of
551 $2.23 \times 10^{-3} s^{-1}$ [31] at room temperature, which we will call Γ_1^{BBR} . The sum of these effects
552 with the rate at which 3P_0 state atoms are lost from the tweezers, Γ_e^t , is in good agreement
553 with the our measured 3P_0 decay rate, $\Gamma_e = \Gamma_e^t + \Gamma_{12}^R + \Gamma_1^{BBR}$ (theory curve in Fig. 2a of the
554 main text).

555 We can compute an expected Ramsey coherence time given these decay rates. Due to the
556 magic-wavelength traps, Rayleigh scattering of the trap light does not cause decoherence [31].
557 As a result, trap-induced scattering only contributes to decay of Ramsey contrast through
558 the Raman scattering processes described above that remove population from the 3P_0 state.

559 Unlike Rayleigh scattering of the trap light, black-body processes that drive population out
560 of and back into the 3P_0 state (predominantly via 3D_1) can serve as an extra source of
561 decoherence that is not directly reflected in the 3P_0 lifetime measurement. Including all
562 these effects, the inferred Ramsey coherence time is:

$$\tau = 2 / (\Gamma_e^t + \Gamma_g^t + \Gamma_{12}^R + \Gamma_1^{\text{BBR}} (1 + \frac{R_0^D}{R_1^D})), \quad (1)$$

563 where Γ_g^t is the ground-state atom loss rate. All of these relevant rates are summarized
564 in extended data table E2. Note that due to the use of ${}^{88}\text{Sr}$ in this work, and given the
565 strength of the magnetic fields used, the effects of spontaneous emission from the clock state
566 are negligible in this analysis.

567 Clock accuracy

568 While a full accuracy evaluation is beyond the scope of this work, the prospects for
569 using the tweezer platform as an absolute frequency reference are fairly good. Many of
570 the dominant systematic effects in tweezer clocks are shared with optical lattice clocks [24],
571 which have accuracies that are currently known at the 10^{-18} level [62]. These effects are
572 discussed in [24], including benefits and drawbacks associated with our use of a bosonic
573 isotope of strontium (${}^{88}\text{Sr}$).

574 The main additional complication in tweezer clocks is the shape of the tweezer potential
575 itself. This yields modified expressions for the light shift [23, 32, 63], and can result in
576 spatially nonuniform polarization [52, 53] which further complicates these calculations. Our
577 work provides a path towards minimizing these effects by operating with optical traps that
578 are shallower than in any other platform. Furthermore, the ability to independently vary
579 the depth of the traps opens up the possibility of performing measurements of the atomic
580 polarizability and hyperpolarizability via synchronous comparisons that take advantage of
581 the high stability demonstrated in this work. Such measurements are, in principle, only
582 limited by QPN and thus can reach arbitrary precision with sufficient averaging time. Based
583 on practical considerations the prospects are good for characterizing these effects at the 10^{-19}
584 level, which would further reduce any inaccuracy imposed by the tweezers.

585 The new scheme for atom preparation presented in this work does not have any impact
586 on accuracy, since the auxiliary potential can be fully extinguished during clock operation.

587 In the case of an asynchronous comparison, the fast state preparation, long lifetimes, and
588 potential for repeated interrogation of the same atomic ensemble in tweezer clocks [23, 24, 44]
589 lead to high duty cycles and thus reduced sensitivity to Dick effect noise in comparison to
590 lattice clocks [24].

591 While the above characteristics are promising, there are a few additional technical con-
592 siderations that could limit the accuracy of current tweezer clocks. While in optical lattice
593 clocks, the lattice mirrors serve as a convenient and robust reference for the atom positions,
594 such a reference does not exist in tweezer clocks due to sensitivity to drifts in the entire
595 tweezer rail (see below). This results in uncompensated Doppler shifts that can limit the
596 atom-laser coherence time, and potentially accuracy, but could be addressed in our current
597 apparatus by taking care to minimize air currents and vibrations in the tweezer system. To
598 date, tweezer clocks have also suffered from inhomogeneous broadening due to slight vari-
599 ations in the optical wavelength of different tweezers [23, 24], as characterized carefully in
600 this work. This is the result of radio frequency offsets imposed by the acousto-optic deflec-
601 tors used to generate the tweezer arrays, and could readily be addressed with alternative
602 technologies, like spatial light modulators, which do not result in such shifts.

603 Atom-laser coherence

604 As a conservative measurement of our atom-laser coherence, we fit the measured Ramsey
605 fringes with frequency as a fixed parameter, which yields a lifetime of 3.6(2) s (Fig. E4).
606 This is consistent with the value of 3.4(4) s measured in our previous work [24].

607 Our 698 nm clock light comes from a laser that is injection locked with light stabilized
608 to a cryogenic silicon reference cavity [8]. The output of this injection lock travels through
609 a 50 m long noise-cancelled fiber. For the Rabi spectroscopy presented in this work, the
610 clock path further included ~ 4 m of fiber and ~ 50 cm of free-space path which were un-
611 cancelled and added phase noise to our clock light. For all remaining data, phase noise
612 cancellation was performed using a reference mirror attached to the objective mount which,
613 to first order, sets the position of the tweezer array. This left only ~ 2 m of un-cancelled
614 fiber in the path, but did not noticeably improve the atom-laser coherence of the system.
615 This suggests that the atom-laser coherence could be limited by drifts of the position of the
616 tweezer array relative to the objective due to air currents in the tweezer rail, or by other

617 uncharacterized sources of noise in our fiber noise cancellation system. We hope to address
618 this shortcoming of the tweezer platform in future upgrades.

619 **Limitations and scaling**

620 The number of traps in this work is limited by thermal lensing in the optical rail used
621 to project the deep 515 nm tweezers, which limits the usable power in the rail to ~ 1.5 W.
622 Given the optical power available at 515 and 813 nm, and the RF bandwidth of the AODs
623 used in the tweezer rail, through more careful material selection and optical design such a
624 system could readily be scaled to more than 1000 traps. Moreover, the approach to scaling
625 laid out in this work is generally applicable to other endeavors in quantum science, where
626 it is useful to reduce the effects of scattering by using a far-detuned science potential, while
627 using a less far-detuned potential for fast, power hungry stages of the experiment which can
628 alleviate constraints on atom number and/or laser power.

629 In our current apparatus, this scaling comes at the cost of relatively high atom loss
630 incurred when imaging in 515 nm potentials [4, 5] compared to the performance possible
631 in 813 nm tweezers [24, 44]. While this is not a significant issue for clock performance,
632 it is relevant for gate or many-body based protocols for generating entanglement, where
633 state purity can be critical. This could be addressed by imaging in a deep 813 nm 3D
634 lattice, which can create tightly confining potentials more efficiently than a tweezer array.
635 Such an approach would have the added benefit of improving our Lamb-Dicke parameter
636 for clock spectroscopy. Given the imaging performance [24, 44] and confinement available
637 in such a potential, single qubit rotations on the clock transition could reach fidelities in
638 excess of 99.9% [32]. In this case a 515 nm tweezer array and axial lattice would still be
639 required for performing high fidelity ground-state cooling via the $^1\text{S}_0 \leftrightarrow ^3\text{P}_1$ transition, and
640 would further be useful for performing site-resolved rearrangement in the lattice. Indeed,
641 preliminary results of loading from a tweezer array into a 2D lattice potential at 813 nm,
642 already integrated into our apparatus, showed that low temperatures were achievable.

643 **Units and errors**

644 Throughout this article and its supplement, unless otherwise stated, all error bars and
645 numerical uncertainties denote a 1σ confidence interval. When we quote a lifetime we are
646 typically referring to the $1/e$ decay time. As a frequency, the inverse of this quantity may
647 be read as radians per second. When we explicitly refer to a Gaussian time constant, we are
648 referring to the timescale associated with 1σ of the Gaussian envelope.

649 **DATA AVAILABILITY**

650 The experimental data presented in this manuscript is available from the corresponding
651 author upon reasonable request. Source data is provided with this paper.

652 **CODE AVAILABILITY**

653 The code used for analysis and simulation in this manuscript is available from the corre-
654 sponding author upon reasonable request.

655 **ACKNOWLEDGEMENTS**

656 We acknowledge fruitful discussions with R. B. Hutson, J. K. Thompson, M. Foss-Feig,
657 S. Kolkowitz, and J. Simon. We further acknowledge F. Vietmeyer and M. O. Brown for
658 invaluable assistance in the design and development of our FPGA-based tweezer control sys-
659 tem. This work was supported by ARO, AFOSR, DARPA, the National Science Foundation
660 Physics Frontier Center at JILA (1734006), and NIST. M.A.N., E.O., and N.S. acknowledge
661 support from the NRC research associateship program.

662 **AUTHOR CONTRIBUTIONS**

663 A.W.Y., W.J.E., M.A.N., N.S., and A.M.K. built and operated the tweezer apparatus,
664 and the silicon-crystal stabilized clock laser was operated by W.R.M., D.K., E.O. and J.Y.
665 All authors contributed to data analysis and development of the manuscript.

666 AUTHOR INFORMATION

667 The authors declare no competing interests.

668 ADDITIONAL INFORMATION

669 Supplementary Information is available for this paper. Correspondence and requests for
670 materials should be addressed to A.M.K. Reprints and permissions information is available
671 at www.nature.com/reprints.

672 EXTENDED DATA

	515 nm	813 nm
Available optical power	10 W	3 W
Ground-state polarizability, α^{E1}	900 a_0^3 [64]	280 a_0^3 [36]
Tweezer $1/e^2$ Gaussian radius	480(20) nm	740(40) nm

TABLE E1. **Relevant optical trapping parameters.** The higher polarizability and available laser power, as well as tighter spatial confinement, make the 515 nm tweezers more appropriate for cooling and imaging atoms in larger tweezer arrays, as these operations require more strongly confining traps.

	Values inferred from measurement (s)
$1/\Gamma_g^t$	101(6)
$1/\Gamma_e^t$	92(5)*
$1/\Gamma_e$	43(4)
Theory values ($\times 10^{-3} \text{ s}^{-1}$)	
$\Gamma_0^{\text{BBR}} ({}^3\text{P}_0 \Rightarrow {}^3\text{P}_0)$	3.45(22) [31]
$\Gamma_1^{\text{BBR}} ({}^3\text{P}_0 \Rightarrow {}^3\text{P}_1)$	2.23(14) [31]
$\Gamma_2^{\text{BBR}} ({}^3\text{P}_0 \Rightarrow {}^3\text{P}_2)$	0.105(7) [31]
$\Gamma_0^{\text{R}} ({}^3\text{P}_0 \Rightarrow {}^3\text{P}_0)$	0.557 (U/E _R) [31]
$\Gamma_{12}^{\text{R}} ({}^3\text{P}_0 \Rightarrow {}^3\text{P}_1, {}^3\text{P}_2)$	0.782 (U/E _R) [31]

TABLE E2. **Rates contributing to the predicted Ramsey lifetime.** All measured values are for a trap depth of 15 E_R, based on interpolating between the nearest points in Fig. 2a of the main text. * indicates that the inferred value of Γ_e^t is dependent on the reasoning and theory values presented in the methods. Note that Γ_2^{BBR} is smaller than the error bars on the other processes, and so we neglect this process in our analysis. U is the trap depth and E_R is the recoil energy of a magic 813 nm photon.

FIG. E1. Sideband cooling and inhomogeneous broadening. The trap frequency and cooling performance in the radial direction is uniform across the entire array — as confirmed by spectra taken along an orthogonal radial axis to the data presented in Fig. 1d of the main text (left). However, in a reduced 6×6 region at the center of the array (denoted by the far-right cartoon), the axial cooling performance is vastly improved (right), with an average phonon occupation of $\bar{n} = 0.00^{+0.06}_{-0.00}$ ($\bar{n} = 0.06^{+0.10}_{-0.06}$) before (after) the handoff. This is due to the comparable extent of the lattice beams to the tweezer array (light-green contour in far-right cartoon shows region over which the lattice intensity stays within 90% of its maximal value).

FIG. E2. Lattice alignment. Measurements of the spatial phase of the standing-wave lattice at each tweezer with an intentional tilt (left) and properly aligned (center) show that it is possible flatten the lattice relative to the entire tweezer array to within 1/10th of a lattice period (histogram, right). This allows for high-fidelity sideband cooling in all axes.

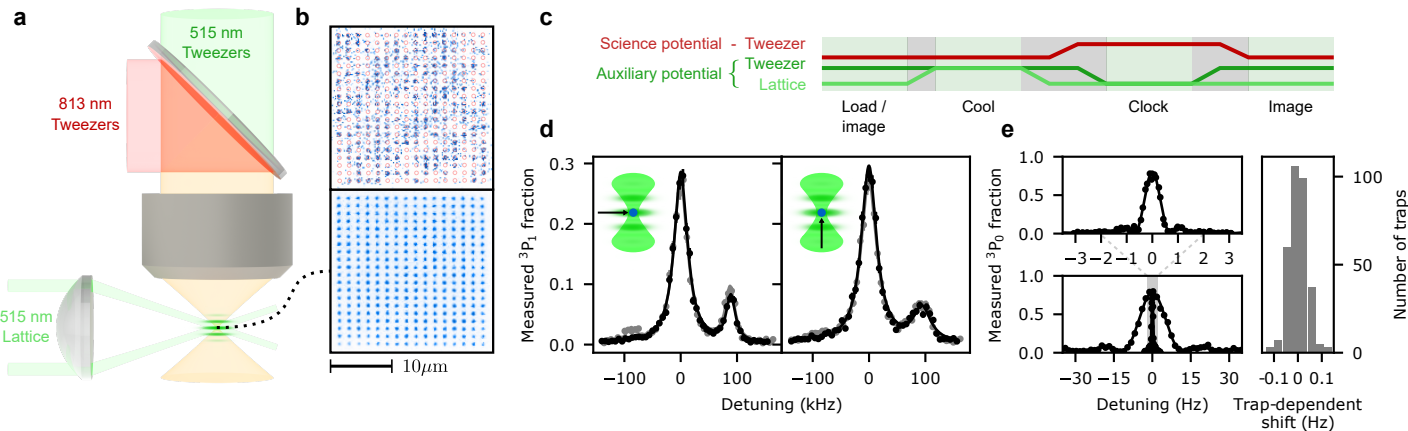
FIG. E3. Timing of experimental sequence. a) The green and black curves track the depths of the 515 nm and 813 nm tweezers, respectively. The colored regions above and below this graph categorize each step of the experiment, which are described in more detail in the methods. We find that maintaining the 813 nm tweezers at a depth greater than $20E_R$ during the ramp down improves the fidelity of the handoff procedure. Not shown is the time required to load atoms into the 515 nm tweezers from the MOTs, which takes roughly 120 ms. b) A zoomed in view of our cooling procedure, showing the depth of the axial lattice. We perform two rounds of sideband cooling, indicated by the two regions shaded in grey. The first, done before ramping up the axial lattice, does not cool axial motion to the ground state. Instead, it is important for reducing the size of the atomic wave packet to ensure loading of a single lattice fringe.

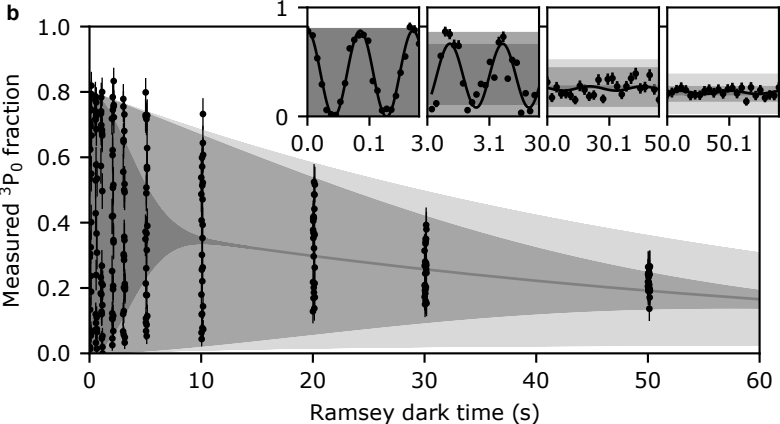
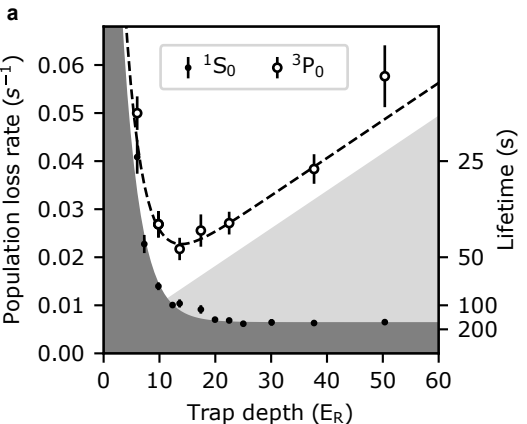
FIG. E4. Measuring atom-laser coherence. Fitting measured Ramsey fringes with fringes of a fixed frequency provides a conservative estimate of atom-laser coherence. Callouts share x-axis units with the main plot, and show the fitted Ramsey data (which is the same data as used in Fig. 2b of the main text)

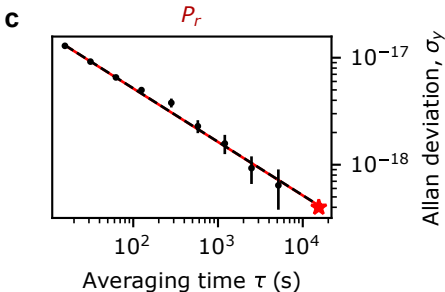
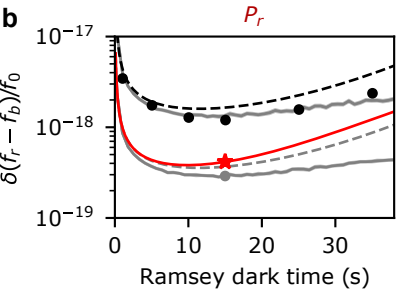
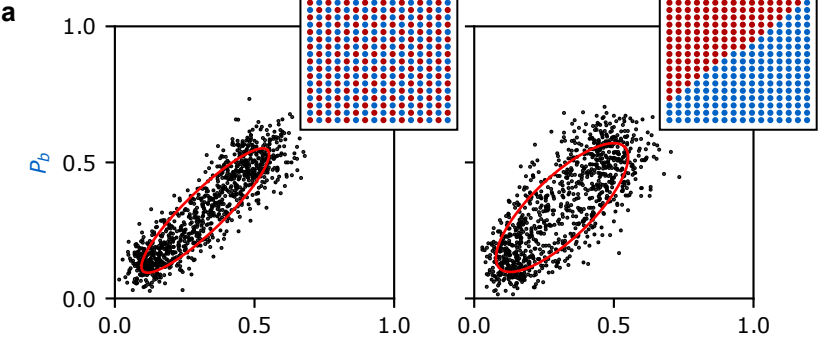
673 * E-mail: adam.kaufman@colorado.edu

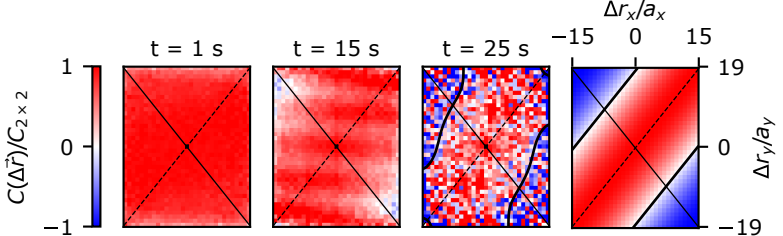
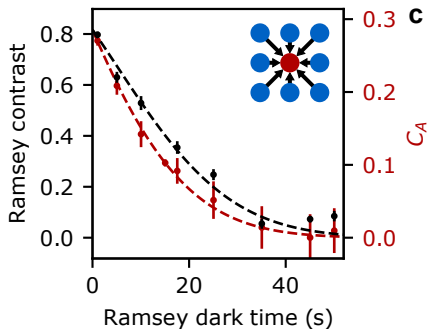
- 674 [51] Monroe, C. *et al.* Resolved-sideband raman cooling of a bound atom to the 3D zero-point
675 energy. *Phys. Rev. Lett.* **75**, 4011–4014 (1995).
- 676 [52] Kaufman, A. M., Lester, B. J. & Regal, C. A. Cooling a single atom in an optical tweezer to
677 its quantum ground state. *Phys. Rev. X* **2**, 041014 (2012).
- 678 [53] Thompson, J. D., Tiecke, T. G., Zibrov, A. S., Vuletić, V. & Lukin, M. D. Coherence and
679 Raman Sideband Cooling of a Single Atom in an Optical Tweezer. *Phys. Rev. Lett.* **110**,
680 133001 (2013).
- 681 [54] Taichenachev, A. V. *et al.* Magnetic field-induced spectroscopy of forbidden optical transitions
682 with application to lattice-based optical atomic clocks. *Phys. Rev. Lett.* **96**, 083001 (2006).
- 683 [55] Bali, S., O’Hara, K. M., Gehm, M. E., Granade, S. R. & Thomas, J. E. Quantum-diffractive
684 background gas collisions in atom-trap heating and loss. *Phys. Rev. A* **60**, R29–R32 (1999).
- 685 [56] Van Dongen, J. *et al.* Trap-depth determination from residual gas collisions. *Phys. Rev. A*
686 **84**, 022708 (2011).
- 687 [57] Mitroy, J. & Zhang, J. Y. Dispersion and polarization interactions of the strontium atom.
688 *Mol. Phys.* **108**, 1999–2006 (2010).
- 689 [58] Gibble, K. Scattering of cold-atom coherences by hot atoms: Frequency shifts from
690 background-gas collisions. *Phys. Rev. Lett.* **110**, 180802 (2013).
- 691 [59] Bothwell, T. *et al.* JILA SrI optical lattice clock with uncertainty of 2.0×10^{-18} . *Metrologia*
692 **56**, 065004 (2019).
- 693 [60] Savard, T. A., O’Hara, K. M. & Thomas, J. E. Laser-noise-induced heating in far-off resonance
694 optical traps. *Phys. Rev. A* **56**, R1095–R1098 (1997).
- 695 [61] Gehm, M. E., O’Hara, K. M., Savard, T. A. & Thomas, J. E. Dynamics of noise-induced
696 heating in atom traps. *Phys. Rev. A* **58**, 3914–3921 (1998).
- 697 [62] Bloom, B. J. *et al.* An optical lattice clock with accuracy and stability at the 10^{-18} level.
698 *Nature* **506**, 71–75 (2014).
- 699 [63] Ovsiannikov, V. D., Pal’chikov, V. G., Taichenachev, A. V., Yudin, V. I. & Katori, H. Multi-
700 pole, nonlinear, and anharmonic uncertainties of clocks of Sr atoms in an optical lattice. *Phys.*
701 *Rev. A* **88**, 013405 (2013).

- 702 [64] Safronova, M. S., Zuhrianda, Z., Safronova, U. I. & Clark, C. W. Extracting transition rates
703 from zero-polarizability spectroscopy. *Phys. Rev. A* **92**, 040501 (2015).







a**b****c**